

# Defect-induced displacement of topological surface state in quantum magnet $\text{MnBi}_2\text{Te}_4$

Felix Lüpke<sup>1,2,3,4,5</sup>, Marek Kolmer<sup>1,6,7</sup>, Hengxin Tan<sup>8</sup>, Hao Chang<sup>1</sup>, Adam Kaminski<sup>6,7</sup>, Binghai Yan<sup>8,9</sup>, Jiaqiang Yan<sup>10</sup>, Wonhee Ko<sup>1,11†</sup>, An-Ping Li<sup>1\*</sup>

<sup>1</sup>*Center for Nanophase Materials Sciences, Oak Ridge National Laboratory, Oak Ridge, Tennessee 37831, USA*

<sup>2</sup>*Department of Materials Science and Engineering, University of Tennessee, Knoxville, Tennessee 37996, USA*

<sup>3</sup>*Peter Grünberg Institute (PGI-3), Forschungszentrum Jülich, 52425 Jülich, Germany*

<sup>4</sup>*Jülich Aachen Research Alliance (JARA), Fundamental of Future Information Technology, 52425 Jülich, Germany*

<sup>5</sup>*Institute of Physics II, Universität zu Köln, Zùlpicher Straße 77, 50937 Köln, Germany*

<sup>6</sup>*Ames National Laboratory, Ames, Iowa 50011, USA*

<sup>7</sup>*Department of Physics and Astronomy, Iowa State University, Ames, Iowa 50011, USA*

<sup>8</sup>*Department of Condensed Matter Physics, Weizmann Institute of Science, Rehovot 7610001, Israel*

<sup>9</sup>*Department of Physics, The Pennsylvania State University, University Park, Pennsylvania 16802, USA*

<sup>10</sup>*Materials Science and Technology Division, Oak Ridge National Laboratory, Oak Ridge, Tennessee 37831, USA*

<sup>11</sup>*Department of Physics and Astronomy, University of Tennessee, Knoxville, Tennessee 37996, USA*

†Correspondence to [wko@utk.edu](mailto:wko@utk.edu)

\*Correspondence to [apli@ornl.gov](mailto:apli@ornl.gov)

## Abstract

The topological magnet  $\text{MnBi}_2\text{Te}_4$  (MBT), with gapped topological surface state, is an attractive platform for realizing quantum anomalous Hall and Axion insulator states. However, the experimentally observed surface state gaps fail to meet theoretical predictions, although the exact mechanism behind the gap suppression has been debated. Recent theoretical studies suggest that intrinsic antisite defects push the topological surface state away from the MBT surface, closing its gap and making it less accessible to scanning probe experiments. Here, we report on the local effect of defects on the MBT surface states and demonstrate that high defect concentrations lead to a displacement of the surface states well into the MBT crystal, validating the theorized mechanism. The local and global influence of antisite defects on the

topological surface states are studied with samples of varying defect densities by combining scanning tunneling microscopy (STM), angle-resolved photoemission (ARPES), and density functional theory (DFT). Our findings identify a combination of increased defect density and reduced defect spacing as the primary factors underlying the displacement of the surface states and suppression of surface gap, shedding light to further development of topological quantum materials.

## Introduction

Topological insulators have an electronically gapped bulk state and topologically protected metallic Dirac surface states. These properties allow to realize the quantum anomalous Hall (QAH) effect by opening a magnetic exchange gap at the Dirac point of the surface states, which can be achieved through introduction of magnetic dopants (e.g., Cr, V) into the topological insulator  $\text{Bi}_{2-x}\text{Sb}_x\text{Te}_3$ [1,2]. However, the random distribution of magnetic dopants in such magnetically doped compounds leads to variations in local magnetism and charge carrier concentration, resulting in inhomogeneous electronic properties on mesoscopic length scales[2]. As a result, the stoichiometric magnetic topological insulator  $\text{MnBi}_2\text{Te}_4$  (MBT) has attracted significant interest: In MBT, magnetic atoms form a well-ordered lattice, resulting in magnetic moments that exhibit ferromagnetic (FM) coupling within each septuple layer and layer-wise antiferromagnetic (AFM) coupling, known as A-type antiferromagnetic coupling[3-9]. This intrinsic magnetic order offers a promising alternative to achieving robust and homogeneous magnetic topological phases.

MBT bulk crystals and thin films have been shown to host a robust bulk band gap with Dirac-like topological surface states. However, the magnetic exchange gaps which open at the surface state Dirac point have been reported with widely varying results, ranging from clearly gapped[5,10-17] to vanishing[16,18-23], which contradicts theoretical predictions[3-5,24-28]. Nonetheless, the QAH effect has been observed in transport experiments[29-35], although typically only at temperatures significantly lower than the Neel temperature  $T_N \sim 25$  K below which the MBT becomes magnetically ordered[29-36] and by application of a magnetic field that forces MBT into a ferromagnetic (FM) phase. The absence of a consistently observed surface gap has been widely debated[8,9,15,18,20,21,37-44], with native antisite defects identified as playing a critical role[15,17,28,37,41,45-48]. While defects are known to induce local variations in the charge carrier concentrations and exchange gaps in MBT, their magnetic moments alone cannot fully account for the reported closing of the exchange gap[15,28]. Recent theoretical work[28] predicts that co-antisite defects, i.e. where a pair of Bi and Mn atoms swap their lattice positions, push the surface state deeper into the crystal bulk, where the surface state interacts with the magnetic moments of the second van der Waals (vdW) layer. Due to the layer-wise AFM order, the magnetic moments of the second vdW layer are opposite to those of the first layer, leading to a suppression of the exchange gap at zero-field. When a magnetic field is applied though, aligning the moments into the FM phase, a sizable exchange gap is recovered, thereby enabling the observation of the QAH effect. So far, confirmation of this prediction in experiments has been challenging, as it requires probing the depth profile of the topological surface states as a function of antisite defect density. Validating and controlling these effects is crucial for further realization of robust magnetic topological phases in MBT.

Here, we resolve the variation of the topological surface state in MBT single crystals with different amounts of antisite defects. At the local scale, scanning tunneling microscopy (STM) reveals a suppression of the surface state due to  $\text{Mn}_{\text{Bi}}$  antisites, with the effect becoming more pronounced as defect density increases. In crystals with a high  $\text{Mn}_{\text{Bi}}$  antisites density, the topological surface state signatures are almost completely absent in STM measurements. However, angle-resolved photoemission spectroscopy (ARPES)

on the same crystals consistently detects pristine topological surface states, regardless of the defect density. We reconcile these seemingly contradicting observations by considering the differing surface sensitivities of these techniques: STM probes the atomic scale surface, whereas ARPES can detect surface states even if they are located a few nanometer below the crystal surface[49]. This interpretation is further corroborated by density functional theory (DFT) calculations, which show that increasing the antisite density pushes the topological surface states away from the crystal surface and deeper into the crystal, where the surface state gap closes, due to the opposite magnetization of the second layer. Our findings highlight the depth of topological states as an important parameter influencing their electronic properties, providing key insights for future studies on magnetic topological materials.

## Body

Using atomically resolved STM, we identify the most common intrinsic defects in MBT,  $\text{Bi}_{\text{Te}}$ ,  $\text{Mn}_{\text{Bi}}$  and  $\text{Bi}_{\text{Mn}}$  antisites, by their distinct appearance in topography images (Fig. 1a-c)[15,17,37,50]. Because of the surface sensitivity of STM, we only detect  $\text{Bi}_{\text{Te}}$  defects in the topmost atomic layer,  $\text{Mn}_{\text{Bi}}$  defects in the second atomic layer below the surface, and  $\text{Bi}_{\text{Mn}}$  in the fourth atomic layer below the surface. As a result,  $\text{Bi}_{\text{Te}}$  defects appear as single atomic features,  $\text{Mn}_{\text{Bi}}$  defects manifest as triangular features due to the Mn atom in the Bi site affecting the three surface Te atoms above it.  $\text{Bi}_{\text{Mn}}$  defects on the other hand extend over multiple unit cells, making individual defects difficult to distinguish. Tunneling spectroscopy of the surface (Fig. 1d) reveals the bulk band gap and the linearly dispersive density of states around the surface state Dirac cone. The Dirac point is identified as the minimum in tunneling conductance at  $E_{\text{D}} = -285$  meV (Fig. 1d), indicating significant electron doping from defects[15,37,40]. However, no clear gap is observed at the Dirac point, despite predictions by theory[3-5,24-27], consistent with previous ARPES[18,20-23] and STM investigations of other MBT crystals[16,17,37].

We perform tunneling spectroscopy and ARPES measurements on two MBT single crystals with different defect concentrations, referred to as sample A and sample B. Measurements on sample A are conducted on comparable single crystals from two different growth batches, whereas measurements on sample B are performed on two crystals from the same growth batch. Figures 2a and 2d present large-area STM topographies of sample A and sample B, respectively, allowing us to determine their defect concentrations by counting distinct defect features and normalizing by the number of atoms in the respective atomic layers. Sample A exhibits defect concentrations of 3.8%  $\text{Mn}_{\text{Bi}}$  antisites and 0.48%  $\text{Bi}_{\text{Te}}$  antisites, comparable to earlier observations[37,50]. In contrast, sample B has a higher Mn content, which on average leads to  $(4.6 \pm 0.5)\%$   $\text{Mn}_{\text{Bi}}$  antisites. In Fig. 2d we focus on an area with a concentration of 8.7%  $\text{Mn}_{\text{Bi}}$  and 0.18%  $\text{Bi}_{\text{Te}}$  to highlight the effect of the increased defect concentration in this sample.

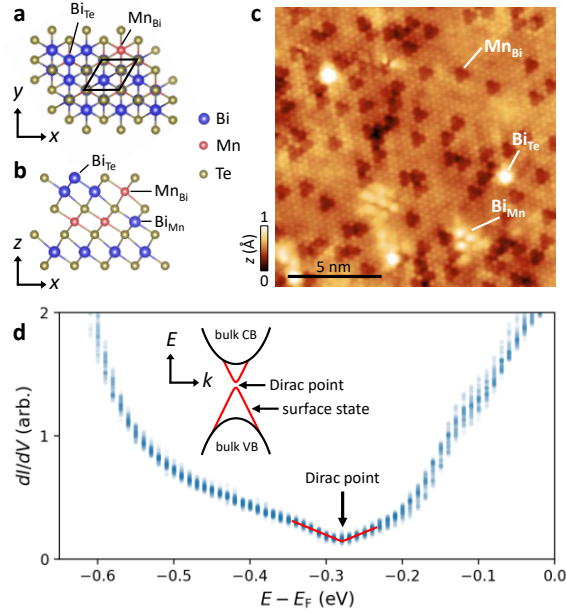


**Figure 1.** Atomic model of MnBi<sub>2</sub>Te<sub>4</sub> viewed from top (a) and side (b) with typical crystal defects. (c) Atomic resolution STM image of the MnBi<sub>2</sub>Te<sub>4</sub> surface with exemplary defect types indicated ( $V_{\text{sample}} = -0.7$  V,  $I_t = 100$  pA). (d) Spatial variations in the tunneling spectrum of the surface, showing the Dirac point at the minimum of the Dirac cone's linear density of states. Inset: Schematic band structure of a magnetic topological insulator.

To quantitatively analyze the electronic properties of both samples in detail, we perform quasi-particle interference (QPI) measurements, obtained via fast Fourier transformation (FFT) of  $dI/dV$  maps recorded at different tunneling bias voltages. These FFT results are then stacked and plotted as a cross-section at each energy  $E - E_F = eV_{\text{sample}}$  (Fig. 2b,e, details in the Supplemental Material). For sample A, the QPI dispersion  $E(q)$  clearly resolves the bulk band gap and surface state Dirac cone, which agrees well with APRES measurements on an identical sample (Fig. 2c). Notably, the doping level between both measurements remains identical. Consistently, neither QPI nor ARPES shows a pronounced surface state gap at the Dirac point. In contrast, sample B presents a markedly different picture, with no clear Dirac dispersion in either STS or QPI. The  $dI/dV$  intensity inside the bulk band gap remains nearly constant and slightly higher than in sample A. On the one hand, this behavior is expected, as defects cause additional scattering and formation of intra-band states that consequently result in suppression of the gap. However, this difference is not reflected in ARPES measurements, which still show a clear Dirac cone (Fig. 2f), though again without an observable surface state gap. The Dirac point energy from ARPES coincides with a local minimum in the  $dI/dV$  spectra, but this minimum is less pronounced than in sample A and is overshadowed by a deeper minimum at -350meV, aligning with the bulk valence band edge according to ARPES. Finally, we note that the doping levels between sample A and B is slightly different, which is expected due to slightly different crystal compositions[15]. However, this doping variation should primarily result in a rigid shift of the band energies without altering the STS spectrum.

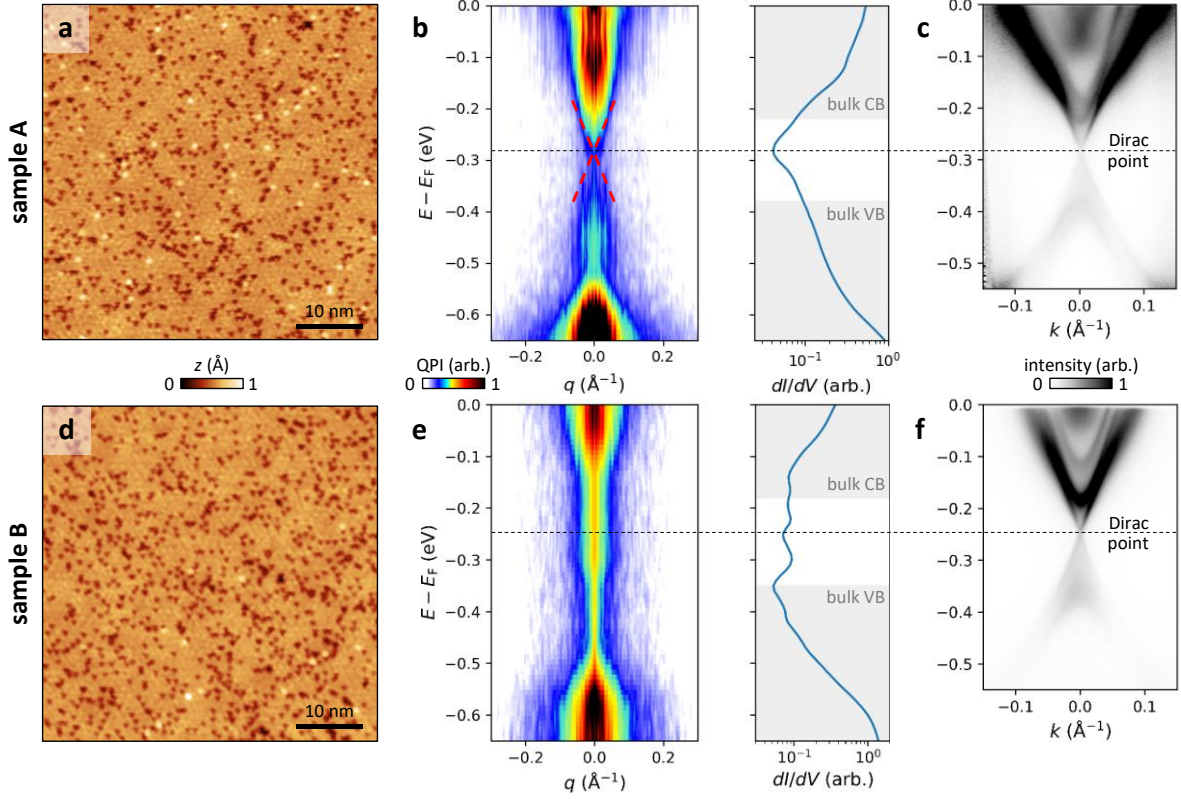


**Figure 2.** (a) STM topography of sample A, where  $\text{Mn}_{\text{Bi}}$  and  $\text{Bi}_{\text{Te}}$  antisites appear as dark and bright dots, respectively. (b) Quasi-particle dispersion obtained from the region shown in panel (a), along with the corresponding averaged  $dl/dV$  spectrum plotted on a semi-logarithmic scale. The horizontal dashed line marks the Dirac point energy and gray shaded areas indicate the bulk valence and conduction bands, as inferred from panel (c). Red dashed lines mark the Dirac dispersion. (c) ARPES spectrum of sample A. (d) STM topography of sample B. (e) Quasi-particle dispersion obtained from the region shown in panel (d), with the corresponding averaged  $dl/dV$  spectrum. (f) ARPES spectrum of sample B. STM scan parameters: (a)  $V_{\text{sample}} = 1 \text{ V}$ ,  $I_t = 100 \text{ pA}$ ; (b),  $V_{\text{sample}} = -0.7 \text{ V}$ ,  $I_t = 1 \text{ nA}$ ; (d),  $V_{\text{sample}} = 1 \text{ V}$ ,  $I_t = 10 \text{ pA}$ ; (e),  $V_{\text{sample}} = -0.7 \text{ V}$ ,  $I_t = 100 \text{ pA}$  for (e). Note the twice larger scale in momentum axis between panels (b,e) and (c,f).

To understand how a twofold increase in  $\text{Mn}_{\text{Bi}}$  antisites leads to drastically different tunneling spectra, we perform a detailed analysis of the STS grid measurements. For sample A, using topographic data, we identify the positions of different defect types (Fig. 3a-d) and compute the average spectra within these regions (see Supplemental Material for details) to determine their effect on the tunneling spectrum (Fig. 3e). It is found that  $\text{Mn}_{\text{Bi}}$  defects, particularly in regions where they cluster, cause a decrease in  $dl/dV$  intensity within the bulk band gap, where the Dirac surface state is identified in Figs. 1 and 2. In contrast,  $\text{Bi}_{\text{Mn}}$  antisites increase the  $dl/dV$  intensity for the surface state.  $\text{Bi}_{\text{Te}}$  antisites, however, show almost no effect on  $dl/dV$  intensity and thus, in the following, we will focus only on  $\text{Mn}_{\text{Bi}}$  and  $\text{Bi}_{\text{Mn}}$  defects. The contrasting effects of  $\text{Mn}_{\text{Bi}}$  and  $\text{Bi}_{\text{Mn}}$  defects become even more apparent when we subtract the average spectrum of the entire scan region from the defect-specific spectra (Fig. 3f), clearly demonstrating their opposite influences on the tunneling characteristics.

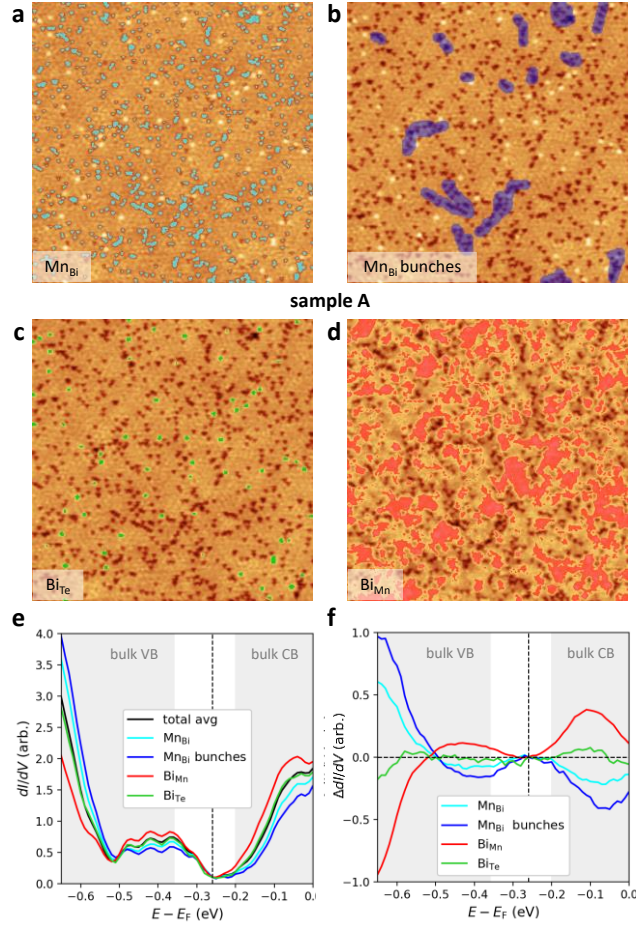


**Figure 3.** (a)-(d) STM topography of  $\text{MnBi}_2\text{Te}_4$  sample A, where regions of different defects are highlighted by color-coded masks. (e) Tunneling spectra averaged in the respective masked areas in (a)-(d). The vertical line indicates the Dirac point energy and gray shaded areas denote the bulk valence and conduction bands. (f) Difference of the curves in (e) with respect to the total average spectrum over the entire scan frame. STM scan parameters:  $V_{\text{sample}} = 1 \text{ V}$ ,  $I_t = 100 \text{ pA}$  for (a)-(d);  $V_{\text{sample}} = -0.7 \text{ V}$ ,  $I_t = 100 \text{ pA}$  for (e) and (f).

We perform the same analysis for sample B, but observe almost no variation of  $dI/dV$  intensity within the bulk gap (Supplemental Fig. 1). This observation suggests that for sample B the tunneling conductance inside the bulk band gap is not affected by the defects visible at the sample surface. Instead, the tunneling conductance likely originates from subsurface defects and bulk carriers[37].

To understand the effect of defects on the surface state LDOS, we perform DFT calculations of MBT with a pair of  $\text{Mn}_{\text{Bi}}$  and  $\text{Bi}_{\text{Mn}}$  antisites in a  $4 \times 4$  supercell (Fig. 4a, b), corresponding to a  $\text{Mn}_{\text{Bi}}$  defect concentration of 3.1% (see Supplemental Material for details). Compared to our previous theoretical work[28], we increase the distance of the  $\text{Mn}_{\text{Bi}}$  and  $\text{Bi}_{\text{Mn}}$  antisites within the unit cell to the 4<sup>th</sup>-next-nearest-neighbor (4N) to isolate their respective effects on the surface state. The resulting calculated STM topography (Fig. 4c) shows that the three Te atoms above the  $\text{Mn}_{\text{Bi}}$  defect appear darker (lower charge density), while the  $\text{Bi}_{\text{Mn}}$  defect produce a more delocalized bright feature (higher charge density), consistent with our STM experiments.

Next, we examine the charge density distributions on the MBT surface, comparing the defect-free surface with the surface containing a 4N co-antisite. In the defect-free crystal, the charge densities of both the surface state valence band (SVB) and surface state conduction band (SCB) are significantly localized in the

topmost septuple layer (SL) (Fig. 4f). Within this first SL, the charge densities show distinct peaks in the surface Te plane, which are expected to dominate the tunneling current to the STM tip, because the tunneling current decays exponentially with increasing distance to the tip ( $\sim 1$  decade per  $\text{\AA}$ ). Thus, we are sensitive to the effect of the defects on the surface state charge density in the topmost atomic plane, since the tunneling contribution of the charge densities below the first atomic plane is orders of magnitude smaller than that from the topmost Te layer.

In the presence of the co-antisite, the charge densities of both SVB and SCB shift toward the second SL, with the centroids of the surface states moving approximately  $1\text{--}2 \text{ \AA}$  downward (Fig. 4g). For both SVB and SCB, the charge density in the surface Te plane is reduced in the presence of the co-antisites, which is expected to result in a smaller tunneling current. We note that this effect is smaller than in a configuration where the two antisites are closer to each other (3N, as discussed in Ref. [28]). Nonetheless, the Dirac gap shrinks compared to the perfect surface, due to the opposite magnetization of the second SL resulting from the interlayer AFM (Fig. 4d,e).

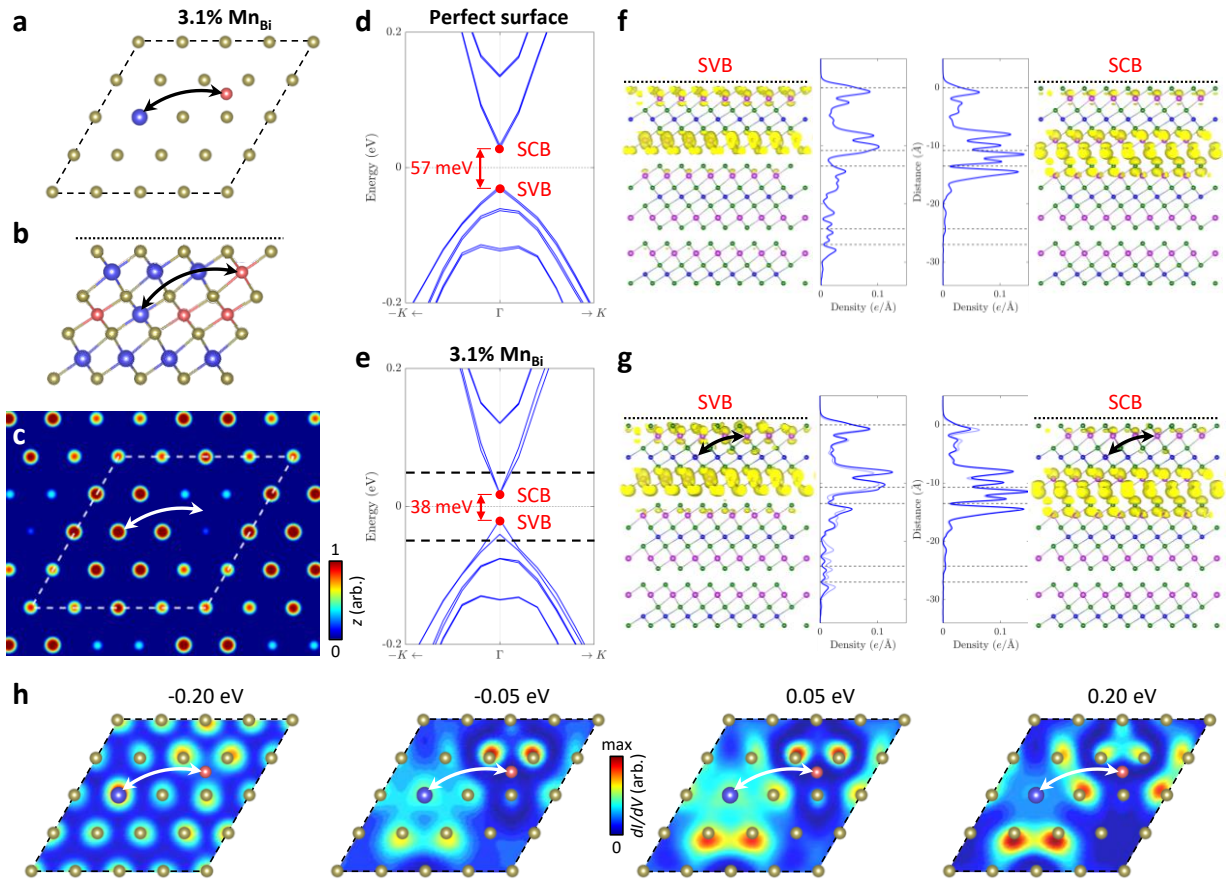


**Figure 4.** (a,b) Schematics of the defect configuration for a 4<sup>th</sup>-next-nearest-neighbor antisite (indicated by arrows). (c) Calculated STM topography at a tip height  $3 \text{ \AA}$  above the surface. (d,e) Calculated band structure of a perfect surface and one with the antisite shown in panels a-c, respectively. (f,g) Charge density distributions for surface state valence band and conduction band for the perfect surface and the defective surface, respectively. The atomic models show the first three MBT septuple layers below the surface (black dotted line) and the superimposed charge distributions of the two bands (yellow isosurfaces, corresponding to  $3.4 \times 10^{-4} e/\text{\AA}^3$ ). The line graphs show the corresponding planar averaged charge density along the out-of-plane direction. In (g) the averaged charge density of the perfect surface is

indicated in light blue. (h) Calculated  $dI/dV$  maps at four different energies, corresponding to the surface state ( $\pm 0.05$  eV, dashed lines in e) and in the bulk bands ( $\pm 0.20$  eV).

To analyze the local effect of the individual defects on the tunneling, we calculate  $dI/dV$  maps for the Dirac bands just above and below the Dirac gap, as well as inside the bulk bands (Fig. 4h). At both energies in the surface states ( $\pm 0.05$  eV), we observe a reduction of the tunneling conductance at the position of the  $Mn_{Bi}$  defect site compared to the defect free surface, while it is enhanced in the vicinity of the  $Bi_{Mn}$  defect. This behavior closely reproduces our STM experiments shown in Fig. 3. In the calculated tunneling conductance maps corresponding to the bulk bands ( $\pm 0.20$  eV), the contrast between the two defect sites is less pronounced and again in qualitative agreement with experiment observations.

## Discussion

Our DFT calculations suggest that the variations of the surface state intensity observed in STM measurements of sample A originate from a combination of local conductance variations (Fig. 4h) and the displacement of the surface state into the bulk near antisites (Fig. 4f,g). In contrast, for sample B, the surface state does not correlate with the defect locations visible on the sample surface, indicating that it lacks significant localization within the first SL. Instead, the surface state is pushed deeper into the bulk crystal, making the shift of the charge density into the bulk the dominant effect. This interpretation is supported by the DFT calculations, which show that a reduction of the antisite distance, as which follows naturally from a higher defect density, results in an even further shift of charge density into the bulk, and thus reducing the surface state gap. This trend can be seen by comparing our 4N and 3N configurations in Ref. [28], as well as  $4 \times 4$  and  $3 \times 3$  supercells in Ref. [28] that correspond to defect densities of 3.1% and 5.6%, respectively. The vertical displacement of the surface states explains almost identical surface band structure observed by ARPES for both sample A and B, which is less sensitive to the depth profile. The absence of a surface band gap in ARPES for both samples indicates that 3.8% of  $Mn_{Bi}$  might be high enough to close the gap on the macroscale.

## Conclusion

We conclude that antisite defects in MBT locally push the surface states into the bulk crystal, with this effect becoming enhanced as the antisites spacing decreases and the overall defect density increases. These two effects are clearly correlated, because, on average, the antisite spacing decreases as the defect density increases. Consequently, as the defect density rises, these effects collectively push the surface state deeper into the crystal bulk, where the opposite magnetization of the second SL diminishes the surface gap in the AFM phase. Our findings indicate that the vertical shift of the topological surface states in MBT, induced by antisites, explains the closing of the surface band gap. Therefore, reducing the density of native antisite defects will be crucial for achieving robust surface states with large Dirac gaps in the AFM phase of MBT. Alternatively, defect engineering may induce a switch to ferromagnetic layer-by-layer magnetization[41,46], which may allow to maintain or even improve the surface state gap when the surface state is pushed into the crystal bulk. In this case, the surface state gap may even be more robust against outside disturbances, due to its buried nature.

#### Data availability

The data supporting the findings of this study are available from the authors upon reasonable request.

#### Code availability

The code used to analyse the data is available from the authors upon reasonable request.

#### Competing interests

The authors declare no competing interests.

#### Acknowledgements

This research was conducted at the Center for Nanophase Materials Sciences, which is a DOE Office of Science User Facility. We acknowledge the assistance of James Burns and Jonathan Poplawsky for focused ion beam milling of the STM tips. F.L. acknowledges funding from the Alexander von Humboldt foundation through a Feodor Lynen postdoctoral fellowship and the Emmy Noether Programme of the DFG (Project No. 511561801). J.Q.Y was supported by the U.S. Department of Energy, Office of Science, Basic Energy Sciences, Division of Materials Sciences and Engineering. M.K. and A.K. acknowledge support from the U.S. DOE, Office of Science, Basic Energy Sciences, Materials Science and Engineering Division at the Ames National Laboratory (M.K. was partially supported through a DOE Early Career Project), which is operated for the U.S. DOE by Iowa State University under Contract No. DE-AC02-07CH11358.

#### References

- [1] C.-Z. Chang *et al.*, *Science* **340**, 167 (2013).
- [2] I. Lee *et al.*, *Proceedings of the National Academy of Sciences* **112**, 1316 (2015).
- [3] D. Zhang, M. Shi, T. Zhu, D. Xing, H. Zhang, and J. Wang, *Physical Review Letters* **122**, 206401 (2019).
- [4] J. Li, Y. Li, S. Du, Z. Wang, B. L. Gu, S. C. Zhang, K. He, W. Duan, and Y. Xu, *Science Advances* **5**, eaaw5685 (2019).
- [5] M. M. Otrokov *et al.*, *Nature* **576**, 416 (2019).
- [6] J. Q. Yan *et al.*, *Physical Review Materials* **3**, 064202 (2019).
- [7] P. Rani, A. Saxena, R. Sultana, V. Nagpal, S. S. Islam, S. Patnaik, and V. P. S. Awana, *Journal of Superconductivity and Novel Magnetism* **32**, 3705 (2019).
- [8] P. M. Sass, J. Kim, D. Vanderbilt, J. Yan, and W. Wu, *Physical Review Letters* **125**, 037201 (2020).
- [9] D. Nevola, H. X. Li, J. Q. Yan, R. G. Moore, H. N. Lee, H. Miao, and P. D. Johnson, *Physical Review Letters* **125**, 117205 (2020).
- [10] S. H. Lee *et al.*, *Physical Review Research* **1**, 012011 (2019).
- [11] A. M. Shikin *et al.*, *Physical Review B* **104**, 115168 (2021).
- [12] A. M. Shikin *et al.*, *Scientific Reports* **10**, 13226 (2020).
- [13] H.-R. Ji, Y.-Z. Liu, H. Wang, J.-W. Luo, J.-H. Li, H. Li, Y. Wu, Y. Xu, and J. Wang, *Chinese Physics Letters* **38**, 107404 (2021).
- [14] F. Lüpke *et al.*, *Physical Review B* **105**, 035423 (2022).
- [15] F. Lüpke, M. Kolmer, J. Yan, H. Chang, P. Vilmercati, H. H. Weitering, W. Ko, and A.-P. Li, *Communications Materials* **4**, 82 (2023).
- [16] W. Ko *et al.*, *Physical Review B* **102**, 115402 (2020).
- [17] M. Garnica *et al.*, *npj Quantum Materials* **7**, 7 (2022).
- [18] Y.-J. Hao *et al.*, *Physical Review X* **9**, 041038 (2019).
- [19] H. Li *et al.*, *Physical Review X* **9**, 041039 (2019).
- [20] Y. J. Chen *et al.*, *Physical Review X* **9**, 041040 (2019).

- [21] P. Swatek, Y. Wu, L.-L. Wang, K. Lee, B. Schrunk, J. Yan, and A. Kaminski, *Physical Review B* **101**, 161109 (2020).
- [22] L. Xu *et al.*, *Science Bulletin* **65**, 2086 (2020).
- [23] Y. Hu *et al.*, *Physical Review B* **101**, 161113 (2020).
- [24] M. M. Otrokov *et al.*, *Physical Review Letters* **122**, 107202 (2019).
- [25] S. Tian *et al.*, *Physical Review B* **102**, 035144 (2020).
- [26] X.-M. Ma *et al.*, *Physical Review B* **102**, 245136 (2020).
- [27] H. Zhong, C. Bao, H. Wang, J. Li, Z. Yin, Y. Xu, W. Duan, T.-L. Xia, and S. Zhou, *Nano Letters* **21**, 6080 (2021).
- [28] H. Tan and B. Yan, *Physical Review Letters* **130**, 126702 (2023).
- [29] Y. Deng, Y. Yu, M. Z. Shi, Z. Guo, Z. Xu, J. Wang, X. H. Chen, and Y. Zhang, *Science*, eaax8156 (2020).
- [30] J. Ge, Y. Liu, J. Li, H. Li, T. Luo, Y. Wu, Y. Xu, and J. Wang, *National Science Review* **7**, 1280 (2020).
- [31] C. Liu *et al.*, *Nature Materials* **19**, 522 (2020).
- [32] D. Ovchinnikov *et al.*, *Nano Letters* **21**, 2544 (2021).
- [33] C. Liu *et al.*, *Nature Communications* **12**, 4647 (2021).
- [34] Z. Ying, S. Zhang, B. Chen, B. Jia, F. Fei, M. Zhang, H. Zhang, X. Wang, and F. Song, *Physical Review B* **105**, 085412 (2022).
- [35] J. Cai *et al.*, *Nature Communications* **13**, 1668 (2022).
- [36] Y. Wang *et al.*, *Nature Communications* **16**, 1727 (2025).
- [37] Z. Huang, M.-H. Du, J. Yan, and W. Wu, *Physical Review Materials* **4**, 121202(R) (2020).
- [38] X. Wu *et al.*, *Physical Review X* **10**, 031013 (2020).
- [39] B. Chen *et al.*, arXiv preprint arXiv:2404.03032 (2024).
- [40] Y. Yuan *et al.*, *Nano Letters* **20**, 3271 (2020).
- [41] Y. Liu *et al.*, *Physical Review X* **11**, 021033 (2021).
- [42] J. Q. Yan, *ECS Journal of Solid State Science and Technology* **11**, 063007 (2022).
- [43] C. Pei *et al.*, *Chinese Physics Letters* **37**, 066401 (2020).
- [44] W.-T. Guo, L. Huang, Y. Yang, Z. Huang, and J.-M. Zhang, *New Journal of Physics* **23**, 083030 (2021).
- [45] Y. Lai, L. Ke, J. Yan, R. D. McDonald, and R. J. McQueeney, *Physical Review B* **103**, 184429 (2021).
- [46] S. Wimmer *et al.*, *Advanced Materials* **33**, 2102935 (2021).
- [47] M.-H. Du, J. Yan, V. R. Cooper, and M. Eisenbach, *Advanced Functional Materials* **31**, 2006516 (2021).
- [48] F. Islam *et al.*, *Advanced Materials* **35**, 2209951 (2023).
- [49] M. P. Seah and W. A. Dench, *Surface and Interface Analysis* **1**, 2 (1979).
- [50] M. Liu, C. Lei, H. Kim, Y. Li, L. Frammolino, J. Yan, A. H. Macdonald, and C.-K. Shih, *Proceedings of the National Academy of Sciences* **119**, e2207681119 (2022).
- [51] J. Q. Yan, S. Okamoto, M. A. McGuire, A. F. May, R. J. McQueeney, and B. C. Sales, *Physical Review B* **100**, 104409, 104409 (2019).
- [52] K. Momma and F. Izumi, *Journal of Applied Crystallography* **44**, 1272 (2011).
- [53] D. Nečas and P. Klapetek, *Open Physics* **10**, 181 (2012).
- [54] I. Lee *et al.*, *Proceedings of the National Academy of Sciences* **112**, 1316 (2015).
- [55] R. Jiang, D. Mou, Y. Wu, L. Huang, C. D. McMillen, J. Kolis, H. G. Giesber, J. J. Egan, and A. Kaminski, *Review of Scientific Instruments* **85** (2014).
- [56] G. Kresse and J. Furthmüller, *Computational Materials Science* **6**, 15 (1996).
- [57] G. Kresse and J. Furthmüller, *Physical Review B* **54**, 11169 (1996).
- [58] J. P. Perdew, K. Burke, and M. Ernzerhof, *Physical Review Letters* **77**, 3865 (1996).

# Supplemental Material - Defect-induced displacement of topological surface state in quantum magnet $\text{MnBi}_2\text{Te}_4$

Felix Lüpke<sup>1,2,3,4,5</sup>, Marek Kolmer<sup>1,6,7</sup>, Hengxin Tan<sup>8</sup>, Hao Chang<sup>1</sup>, Adam Kaminski<sup>6,7</sup>, Binghai Yan<sup>8,9</sup>, Jiaqiang Yan<sup>10</sup>, Wonhee Ko<sup>1,11†</sup>, An-Ping Li<sup>1\*</sup>

<sup>1</sup>*Center for Nanophase Materials Sciences, Oak Ridge National Laboratory, Oak Ridge, Tennessee 37831, USA*

<sup>2</sup>*Department of Materials Science and Engineering, University of Tennessee, Knoxville, Tennessee 37996, USA*

<sup>3</sup>*Peter Grünberg Institute (PGI-3), Forschungszentrum Jülich, 52425 Jülich, Germany*

<sup>4</sup>*Jülich Aachen Research Alliance (JARA), Fundamental of Future Information Technology, 52425 Jülich, Germany*

<sup>5</sup>*Institute of Physics II, Universität zu Köln, Zùlpicher Straße 77, 50937 Köln, Germany*

<sup>6</sup>*Ames National Laboratory, Ames, Iowa 50011, USA*

<sup>7</sup>*Department of Physics and Astronomy, Iowa State University, Ames, Iowa 50011, USA*

<sup>8</sup>*Department of Condensed Matter Physics, Weizmann Institute of Science, Rehovot 7610001, Israel*

<sup>9</sup>*Department of Physics, The Pennsylvania State University, University Park, Pennsylvania 16802, USA*

<sup>10</sup>*Materials Science and Technology Division, Oak Ridge National Laboratory, Oak Ridge, Tennessee 37831, USA*

<sup>11</sup>*Department of Physics and Astronomy, University of Tennessee, Knoxville, Tennessee 37996, USA*

†Correspondence to [wko@utk.edu](mailto:wko@utk.edu)

\*Correspondence to [apli@ornl.gov](mailto:apli@ornl.gov)

## Methods

### Sample preparation

MBT was grown using a flux method, producing single crystals of dimension 3×4 mm and a thickness 0.1–1 mm[51]. The stoichiometry of the crystals was determined using energy-dispersive x-ray analysis, which did not show any compositional variation as function of position on the crystal or between crystals from the same batch. The crystals were cleaved in the UHV chamber at room temperature and a pressure of  $\sim 10^{-10}$  mbar just before the introduction to the STM stage for characterization. Measurements on multiple cleaves and positions on the sample show consistent crystal quality. Photoemission and transport measurements on samples of similar composition have shown a transition temperature of  $T_N \sim 24$  K and

non-closing of the surface state gap through the magnetic transition[9,51]. The crystal structures in Fig. 1 were created using VESTA[52].

### Scanning Tunnelling Microscopy/Spectroscopy

The STM/S experiments were performed in two ultra-high vacuum (UHV) systems (base pressure  $\sim 10^{-10}$  mbar) hosting commercial low-temperature scanning tunnelling microscopes (Scienta Omicron LT-Nanoprobe and LT-STM), both operating at liquid helium temperatures ( $\sim 5$  K). PtIr and W tips were obtained by electromechanical etching. PtIr tips were further sharpened by focus ion beam milling. All tips were conditioned by indentation into Au(111) surfaces, where the Shockley surface state was used as a benchmark for a clean tip spectrum.  $dI/dV$  spectra were acquired using standard lock-in techniques at oscillation amplitudes of a few mV. Thermal broadening of the tunnelling spectra ( $5 k_B T \approx 2$  meV) does not have a significant effect on our tunnelling spectra. The spectroscopy maps in Figs. 2 and 3 were recorded on a  $256 \times 256$  px<sup>2</sup> grid.

We detect the different defect types in Fig. 3 using threshold detection based on their topographic heights. To do so, we first apply plane correction to the STM topographies and set their minimum height to 0 pm. Then, we consider positive bias voltage scans, where Bi<sub>Te</sub> defects exhibit the greatest topographic height, allowing us to detect them using a threshold that includes only data points above 73 pm (Fig. 3c). In the same scans, Mn<sub>Bi</sub> defects appear as threefold depressions on the surface, because the three Te atoms that sit on top of the Mn antisite atoms have lower electronic contrast[15,37]. We thus set a threshold that includes only data points below 40 pm (Fig. 3a). Mn<sub>Bi</sub> defect bunches are identified manually, selecting regions where multiple such defects are clustered together, without applying threshold detection (Fig. 3b). To detect Bi<sub>Mn</sub> antisites, we analyze scans at negative bias voltage, where these defects appear as bright, cloud-like features[37], and set a threshold that includes data points above 43 pm (Fig. 3d). Topography data visualization and threshold detection were done using Gwyddion[53].

### Quasiparticle interference

We calculate QPI patterns from  $dI/dV$  grid spectroscopy maps by performing a Fourier transformation,  $dI/dV(x, y, E) \rightarrow \overline{dI/dV}(q_x, q_y, E)$ , where  $q_x, q_y$  are aligned with the high symmetry axes of the atomic lattice. For MBT, the QPI reproduces the dispersion of the gapped Dirac cone,  $E_{\pm}(k) = E_D \pm \sqrt{(\hbar v_F k)^2 + \Delta^2}$ , where  $v_F$  is the Fermi velocity,  $E_D$  is the Dirac point energy (i.e. the doping level, and  $\Delta$  is the magnetic exchange gap[54], and scattering vector  $q = 2k$ .

### Angle-resolved photoemission spectroscopy

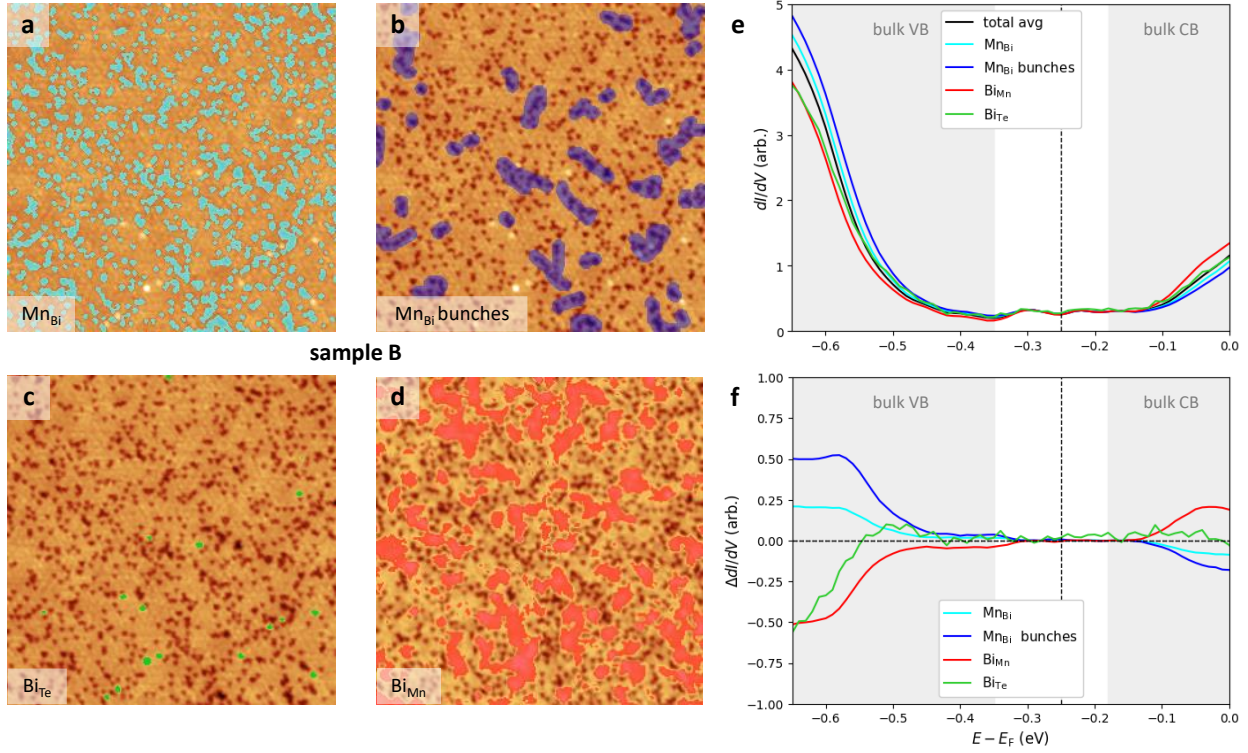
Samples used for ARPES measurements were cleaved *in situ* at 60 K under ultrahigh vacuum. The data were acquired using a tunable vacuum ultraviolet laser ARPES system that consists of an Omicron Scienta DA30 electron analyzer, a picosecond Ti:sapphire oscillator, and a fourth harmonic generator[55]. Data were collected with photon energies of 6.7 and 6.36 eV. Momentum and energy resolutions were set at  $\sim 0.005$  Å<sup>-1</sup> and 2 meV. The size of the photon beam on the sample was  $\sim 15$  μm.

### Density Functional Theory

All the calculations were performed within density functional theory as implemented in Vienna *ab initio* simulation package[56,57]. The generalized gradient approximation describes the exchange-correlation interaction as parametrized by Perdew-Burke-Ernzerhof[58]. The cutoff energy was 350 eV for the plane wave basis. The Mn *d* electrons were treated with a Hubbard *U* of 5 eV. The surface band structures under different surface co-antisites were simulated with slab models of 5-SL thick. The in-plane supercell was examined from 2x2 to 4x4 to investigate the antisite density effect. Three different magnetic

configurations were considered: (i) FM, where all magnetic moments are parallel; (ii) *A*-type AFM, where the  $Mn_{Bi}$  moment is parallelly coupled to other magnetic moments in the same SL; and (iii) Ferri-AFM, where the  $Mn_{Bi}$  moment is antiparallel to other moments in the same SL in the *A*-type AFM framework (see Ref. [28] for details).

Region averaged spectra of sample B



**Supplemental Figure 1.** Same as Fig. 3 but for sample B. (a)-(b)STM topography of MnBi<sub>2</sub>Te<sub>4</sub> sample B, where regions of different defects are highlighted by color-coded mdrasks. (e) Tunneling spectra averaged within the respective masked areas in (a)-(d). The vertical line indicates the Dirac point energy and gray shaded areas denote the bulk valence and conduction bands. (f) Difference of the curves in (e) with respect to the total average spectrum over the entire scan frame. STM scan parameters:  $V_{\text{sample}} = 1$  V,  $I_t = 100$  pA for (a)-(c), and  $V_{\text{sample}} = -0.7$  V,  $I_t = 100$  pA for (d)-(f).